remote sensing

MDPI

Article

Altimeter Observation-Based Eddy Nowcasting Using an Improved Conv-LSTM Network

Chunyong Ma [1,2], Siqing Li [1], Anni Wang [1], Jie Yang [1,2] and Ge Chen [1,2,*]

[1] College of Information Science and Engineering, Ocean University of China, 238 Songling Road, Qingdao 266100, China; chunyongma@ouc.edu.cn (C.M.); lisiqing@stu.ouc.edu.cn (S.L.); wanganni@stu.ouc.edu.cn (A.W.); yangjie2016@ouc.edu.cn (J.Y.)

[2] Laboratory for Regional Oceanography and Numerical Modeling, Qingdao National Laboratory for Marine Science and Technology, No.1 WenHai Road, Qingdao 266200, China

* Correspondence: gechen@ouc.edu.cn; Tel.: +86-532-66781812

Received: 15 January 2019; Accepted: 28 March 2019; Published: 1 April 2019

Abstract: Eddies can be identified and tracked based on satellite altimeter data. However, few studies have focused on nowcasting the evolution of eddies using remote sensing data. In this paper, an improved Convolutional Long Short-Term Memory (Conv-LSTM) network named Prednet is used for eddy nowcasting. Prednet, which uses a deep, recurrent convolutional network with both bottom-up and top-down connects, has the ability to learn the temporal and spatial relationships associated with time series data. The network can effectively simulate and reconstruct the spatiotemporal characteristics of the future sea level anomaly (SLA) data. Based on the SLA data products provided by Archiving, Validation, and Interpretation of Satellite Oceanographic (AVISO) from 1993 to 2018, combined with an SLA-based eddy detection algorithm, seven-day eddy nowcasting experiments are conducted on the eddies in South China Sea. The matching ratio is defined as the percentage of true eddies that can be successfully predicted by Conv-LSTM network. On the first day of the nowcasting, matching ratio for eddies with diameters greater than 100 km is 95%, and the average matching ratio of the seven-day nowcasting is approximately 60%. In order to verify the performance of nowcasting method, two experiments were set up. A typical anticyclonic eddy shedding from Kuroshio in January 2017 was used to verify this nowcasting algorithm's performance on single eddy, with the mean eddy center error is 11.2 km. Moreover, compared with the eddies detected in the Hybrid Coordinate Ocean Model data set (HYCOM), the eddies predicted with Conv-LSTM networks are closer to the eddies detected in the AVISO SLA data set, indicating that deep learning method can effectively nowcast eddies.

Keywords: remote sensing data; mesoscale oceanic eddies; deep learning; convolution LSTM network

1. Introduction

Mesoscale eddies can be defined as rotating water masses that play an important role in the transport of marine materials [1]. Eddies are widely distributed around the world. Scientists have conducted many studies on eddies in different regions [2–15]. Accurately forecasting the properties and trajectories of mesoscale eddies not only plays an important role in the study of understanding eddy propagation and eddy evolution characteristics, but also has important scientific significance and application value for improving the simulations and predictions of regional weather and climate change.

In general, mesoscale eddies are forecasted based on numerical ocean models combined with data assimilation methods and historical observations. In 1984, Robinson et al. [16] published the first mesoscale eddy forecast using an observation network, a statistical model of an anisotropic mixed

space-time target analysis scheme, and a dynamic model of the baroclinic quasi-ground rotation associated with airflow. They successfully predicted the merging, weakening, and disappearance of an anticyclonic eddy in the California ocean current system over a two-week period and the enlarging and strengthening of another cyclonic eddy. In 1994, Masina and Pinardi [17] presented a quasi-geostrophic numerical model of the initial field of the Adriatic Sea region with a regular grid through objective analysis technology and made a 30-day dynamic prediction of an eddy in the eddy field. They found that topography changes had a considerable impact on the prediction ability of the model. Shriver et al. (2007) [18] increased the resolution of the forecasting system from 1/16° [19] to 1/32° based on the Navy Layered Ocean Model (NLOM) combined with an optimal interpolation (OI) method to perform a 30-day forecast each week. Based on a comparison of ocean water color images of the Northwest Arabian Sea and Gulf of Oman, the prediction error of the system for mesoscale eddies was quantitatively evaluated.

The forecasting of eddies with numerical models varies from qualitative forecasts to quantitative forecasts, and certain limitations remain for both approaches. Forecasts are generally only effective when the topography changes are sufficiently small. The nonlinear characteristics of mesoscale eddies and the sensitivity of forecasting to the initial conditions of models make eddies difficult to forecast. Additionally, background error can influence eddy predictions. Data assimilation can provide the initial conditions for forecasting but does not compensate for the shortcomings of most models.

In this paper, we use satellite altimeter data combined with deep learning networks to nowcast mesoscale eddies. Marine remote sensing technology, such as satellite altimeters, has become an important method of eddy observation. Eddies have been studied both intensively and extensively with long-term mesoscale eddy data series. Satellite altimeter data can be used to study the radius, energy, and evolution of eddies [20–22]. Few studies have been conducted to forecast future eddies using previous SLA data. Additionally, data mining methods, such as deep learning, are rapidly evolving. Driven by data and the ability to automatically extract features (knowledge) from data, this method has significant advantages in analyzing unstructured, uncertain, and variable data sets across multiple fields. Deep learning algorithms have been used for oceanographic applications such as classification, identification, and prediction. Lima et al. (2017) [23] used convolutional neural networks to identify ocean fronts, and this approach yielded a higher recognition accuracy than did traditional algorithms. Yang et al. (2018) [24] established a sea surface temperature (SST) prediction model based on LSTM networks that has been well tested using China's coastal SST data set. Because eddies are influenced by multiple factors, it is very difficult to extract the characteristics and trends associated with the nonlinear evolution of eddies. Deep learning can be applied to convert complex processes into simple expressions, making it suitable for eddy nowcasting.

In order to compare predictions with real values to evaluate nowcasting methods, this paper uses previous observation data to conduct experiments. Based on 26-year global coverage and high-resolution satellite altimeter SLA time series from the AVISO project, an improved Conv-LSTM neural network is applied for future SLA data reconstruction and prediction according to the intrinsic structure and trends of the SLA data. Combined with an eddy detection algorithm, future eddy properties can be forecasted (Figure 1).

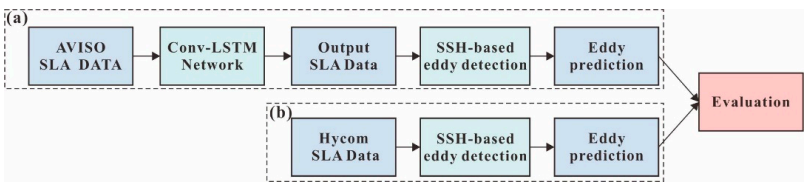

Figure 1. Workflow: (**a**) Training the Conventional Long Short-Term Memory (Con-LSTM) network and performing eddy detection to nowcast the future eddy parameters; (**b**) Identifying the eddy signals from HYCOM model data. Comparison and analyzing the eddy detection results.

This paper is structured as follows. The second section introduces the data set, method, and technology used for eddy nowcasting, including the SLA data set, improved Conv-LSTM network

and eddy detection algorithm. The third section presents the details of the experiment and results. The fourth section discusses the comparison of nowcasting performance with HYCOM data and a nowcasting example of a single anticyclonic eddy, and a summary is given in the fifth section.

2. Materials and Methods

The two most important requirements for the implementation of deep learning algorithms are sufficient data and appropriate models. First, the 26-year (1993–2018) daily gridded SLA data from the AVISO (http://www.aviso.oceanobs.com) were used in this study. The data set was mainly composed by fusing the information obtained from multiple altimeter satellites (ERS-1/2, Topes/Poseidon, ENVISAT and Jason-1/Jason-2). The SLA data are gridded with a 0.25° Mercator projection grid that covers areas between 0°E–360°E and 90°S–90°N. The fused data from multisatellite altimeters have high temporal and spatial resolutions, which make them beneficial for detecting mesoscale eddy signals. Second, recent advances in deep learning, especially Recurrent Neural Networks (RNNs) and Long Short-Term Memory (LSTM) models [25–27], have improved time series-based predictive models. Compared to the normal FC-LSTM model, the improved Conv-LSTM network [28] can continuously predict SLA data with top-down and bottom-up connections. The prediction is continuously performed, and the error propagates forward so that the model can better simulate and reconstruct spatiotemporal relationships and predict SLAs. Based on the SLA prediction results, SLA-based eddy identification technology [29] is used to achieve the nowcasting of eddies. The improved Conv-LSTM network and SLA-based eddy identification techniques will be introduced in Sections 2.1 and 2.2, respectively.

In this experiment, the South China Sea (105–125°E and 5–25°N) was selected as the experimental area for eddy nowcasting. Oceanographers conducted extensive scientific research on the spatiotemporal characteristics and the dynamic mechanisms of eddies in the South China Sea using remote sensing observation data [30–32]. The overall spatiotemporal variability of the South China Sea eddies has become increasingly clear. In the South China Sea, the eddies mainly propagate southwestward along the continental slope. In the central region, the eddies exhibit slight divergence but generally move to the west [33]. The eddies in the South China Sea display strong propagation regularity, making them suitable target eddies for nowcasting experiments. The density distribution of numbers of eddies has been shown in Figure 2.

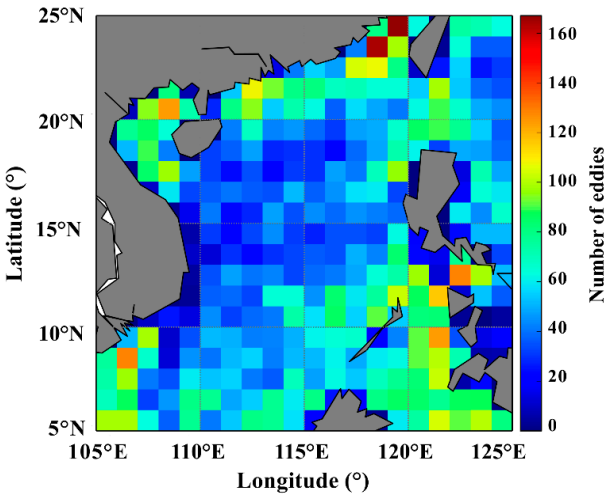

Figure 2. The density distribution of numbers of eddies in the South China Sea from January 1993 to December 2016.

2.1. An Improved Conv-LSTM Network

Mesoscale ocean eddy nowcasting uses previously observed SLA data sequences to predict future SLA data in a local area (such as the South China Sea) and then extracts the mesoscale eddy signals

from the SLA prediction results based on eddy detection algorithms. In practice, an SLA image can be obtained every other day, and future K SLA maps can be predicted given the previous J observations. In machine learning, this process can be seen as a spatiotemporal sequence prediction problem.

In the nowcasting of mesoscale ocean eddies, we observe a dynamic SLA system over time, recording P measurements in an M × N grid. From a spatial perspective, the observations at any time can be represented as a tensor $X \in R^{P*M*N}$. From a temporal perspective, the observations can be expressed as a sequence of tensors over time, X_1, X_2, ..., X_T. The spatiotemporal prediction problem can be seen as the most likely result of a K-length sequence of future SLAs based on the previous J observations.

$$X_{t+1}, \ldots, X_{t+K} = \underset{X_{t+1} \ldots, X_{t+K}}{\operatorname{argmax}} \; p(X_{t+1} \ldots, X_{t+K} | X_{t-J+1} \ldots, X_t) \tag{1}$$

Compared to standard LSTM, Conv-LSTM can model space-time structures by encoding geographic information as tensors, thereby overcoming the limitation of losing spatial information in standard LSTM networks. Therefore, the Conv-LSTM network makes it possible to consider the overall SLA information in the prediction. Eddies are highly nonlinear [22]. The prevalence of coherent mesoscale features (referred to here as eddies) readily apparent in these high-resolution SLA fields. LSTM layer can capture the temporal relationship, i.e., they regulate variation among the time series SLA data. At the convolutional layer, feature extraction is performed on SLA data by different convolution kernels which are selected randomly, and information useful for prediction such as gradient of SLA is extracted. The potential information contained in SLA data can be learned by the network and used to predict the future SLA. Based on the Conv-LSTM concept, the network structure is enhanced to construct an improved Conv-LSTM named the Prednet model for predicting sequences of images [34]. A structure in which the error is fed forward is added to the network, as shown in Figure 3. The network consists of a series of repeatedly stacked blocks, each of which can be viewed as a layer. Each block contains four basic parts: an input convolutional layer Al, a recursive representation layer Rl, a prediction layer $\hat{A}$l, and an error representation layer El. The horizontal expansion of all modules is an expansion of time.

$$\begin{gathered} A_l^t = \begin{cases} x_t & if\ l = 0 \\ MAXPool\Big(RELU\Big(CONV\Big(E_{l-1}^t\Big)\Big)\Big) & l > 0 \end{cases} \\ \hat{A}_l^t = RELU\big(CONV\big(R_l^t\big)\big) \\ E_l^t = [RELU(A_l^t - \hat{A}_l^t); RELU(\hat{A}_l^t - A_l^t)) \\ R_l^t = CONVLSTM\Big(E_l^{t-1}, R_l^{t-1}, UPSAMPLE\Big(R_{l+1}^t\Big)\Big) \end{gathered} \tag{2}$$

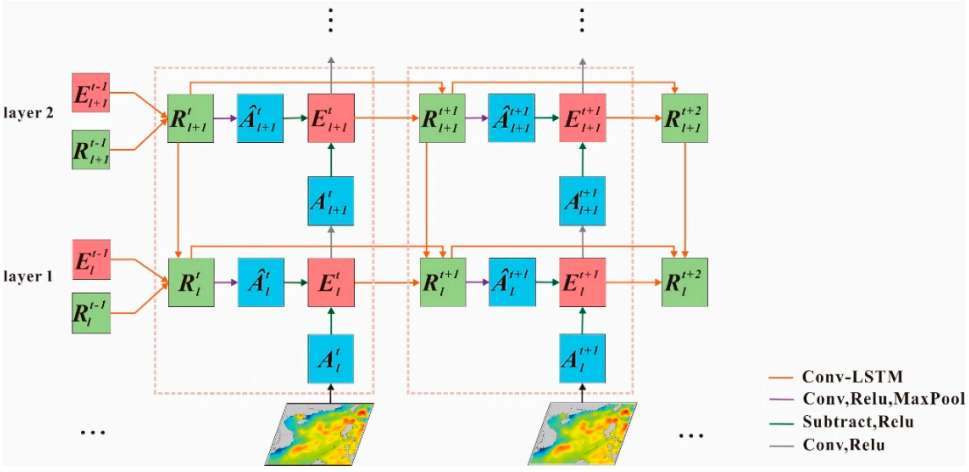

Figure 3. Architecture of the improved Conv-LSTM network.

2.2. Eddy Detection

In 2016, Liu et al. proposed an eddy detection algorithm based on the radius, amplitude, eddy core, and closed SLA contour lines to describe an eddy structure with maximum average geostrophic velocity. Figure 4 shows a flowchart detailing the parallel eddy detection algorithm. The global SLA map is first divided into regions (partitions). Second, spatial high-pass filtering is performed for the SLA mapping of each region. Third, the local extreme SLA pixels are scanned, and the extreme pixels are specified as eddy seeds. Fourth, the SLA contours are searched, and the eddy boundaries are extracted (SLA contour calculations and iterations). Finally, all the current eddy recognition results from the SLA maps in these regions are seamlessly merged into a global eddy current map (regional eddy result merging).

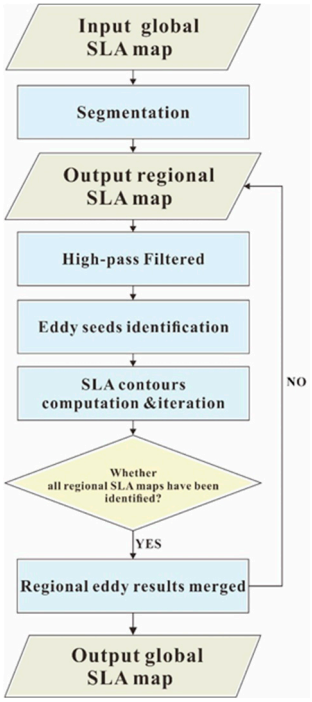

Figure 4. Flowchart of eddy detection method.

3. Experiment and Results

AVISO provides SLA time delay data from 1993–2016. The data from 2006 and 1997 were arbitrarily selected as the verification set, and data from the remaining 22 years were used as the training set. The SLAs corresponding to the gridded data in the South China Sea region of 105–125°E and 5–25°N were extracted, and the corresponding image data sets were constructed. Each image was an 80 × 80 single-channel greyscale image of the corresponding region. The value of each pixel represents the value of the SLA at that location.

3.1. Model Training and Testing

The training data set was used for training the SLA prediction model. In the process of model training, the dimensions of the input matrix were (8036, 80, 80), where 8036 was the SLA data set size over 8036 days for the training set and 80*80 was the SLA grid size. The convolution kernel size was (3, 3, 3). The number of training runs was 80 epochs, and each epoch included 1600 batches. If the learning rate is too high, the algorithm may struggle to converge. Conversely, if the learning rate is too low, the algorithm will take longer to converge. In this experiment, we set the dynamic learning rate to 0.001 before 75 epochs and adjusted it to 0.0001 after 75 epochs. The Prednet model was trained with loss only in the lowest layer, deemed Prednet L_0. The model was trained with 0.1 weights in the upper

layers, deemed Prednet L_{all}. In the SLA nowcasting experiment, the L_0 model can converge faster with a smaller loss value when it tends to be stationary, and the accuracy of the model is high based on this approach. Finally, the L_0 model was chosen in the experiment.

The model used in this paper is a one-step prediction model based on past observation data. There are two ways to perform multiple-step prediction. The first approach is a recursive method, in which the predicted values are used as inputs for the next prediction. The other method is to predict the value at the next step by adding the predicted value to the training set. The recursive method is influenced by error accumulation. The retraining method, which is more suitable for adding new data to the model, will produce relatively good prediction results, but it requires extensive calculations during the training process. In the experiment, the recursive method is used to predict the SLA maps over the seven days after the current time step.

3.2. SLA Prediction Evaluation

In this experiment, SLA data observed over 30 days were used to predict the values over the subsequent seven days. Real observations from the previous 30 days are used as the input to output a prediction for the first day. Then, the first day prediction is added to the input data set, and the second day prediction is output. This process is then repeated for seven days. The results on August 2, which are based on the predictions from the first day to the seventh day, are shown in Figure 5. Figure 6 is the error map of the predicted SLA values compared to the real observed values on August 2. To quantitatively evaluate the prediction capability of the model for mesoscale eddies, the root mean square error (RMSE) of SLAs was used. The RMSE definition is given in Equation (3), where y_i is the true SLA value and $\hat{y}_i$ is the predicted SLA value.

$$RMSE = \sqrt[2]{\frac{1}{m}\sum_{i=1}^{m}(y_i - \hat{y}_i)^2} \tag{3}$$

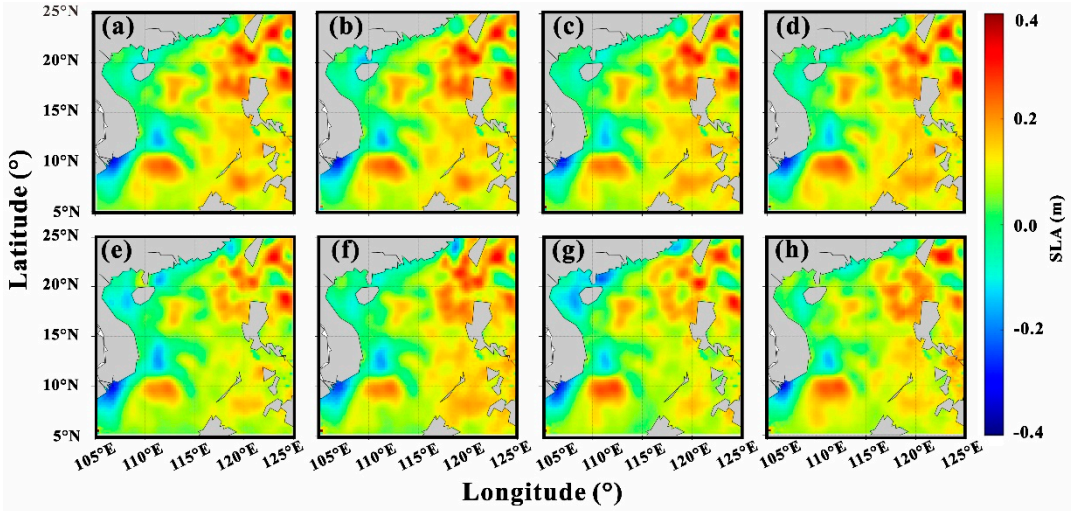

Figure 5. SLA prediction result maps for August 2, 2018. (**a**) The SLA altimetry map on August 2. (**b**–**h**) The SLA predictions from the first day to the seventh day.

Figure 7 shows the RMSE distribution in each grid during the test. On the first three days of the prediction (Figure 7a–c), the SLA prediction errors are very small, and the predictions remain close to the real values. Over time, the SLA RMSE gradually increases, and the regional average RMSE gradually increases from 0.96 cm on the first day to 3.28 cm on the seventh day. The southern South China Sea was considered as 5°N–15°N, where the regional average RMSE is 1.93 cm, and the regional average RMSE of northern South China Sea (15°N–25°N) is 2.39 cm. The extreme errors are mainly distributed in marginal land areas and the northern South China Sea. Notably, the error distribution of

SLA is in line with the area where the sea level changes dramatically in the south China sea region. Generally, sea level changes dramatically in the area where the water depth is shallower, and the sea area northwest of Luzon island in the south China sea.

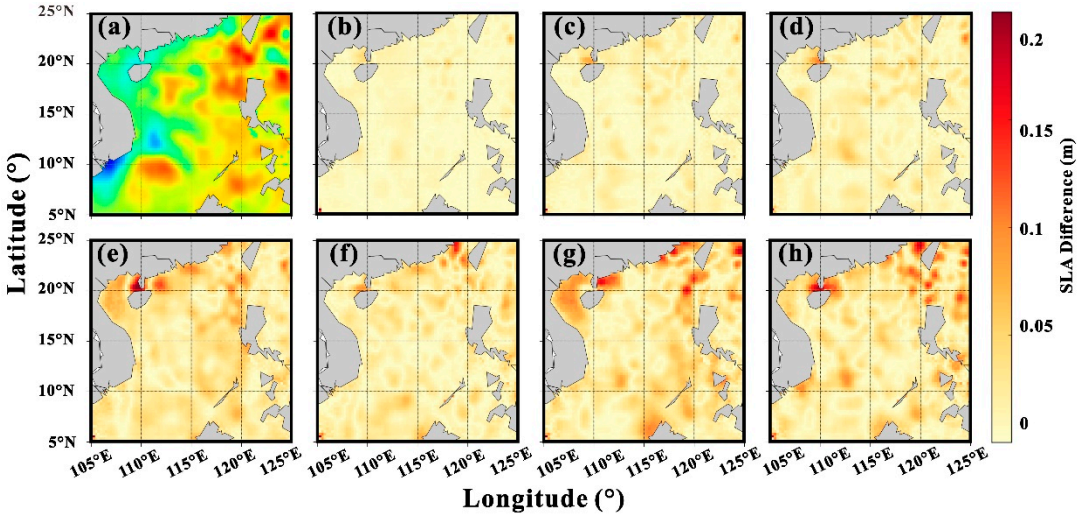

Figure 6. Error maps of the SLA predictions on August 2, 2018. (**a**) The SLA altimetry map on 2 August. (**b**–**h**) The differences between the true values and predicted values from the first day to the seventh day of prediction.

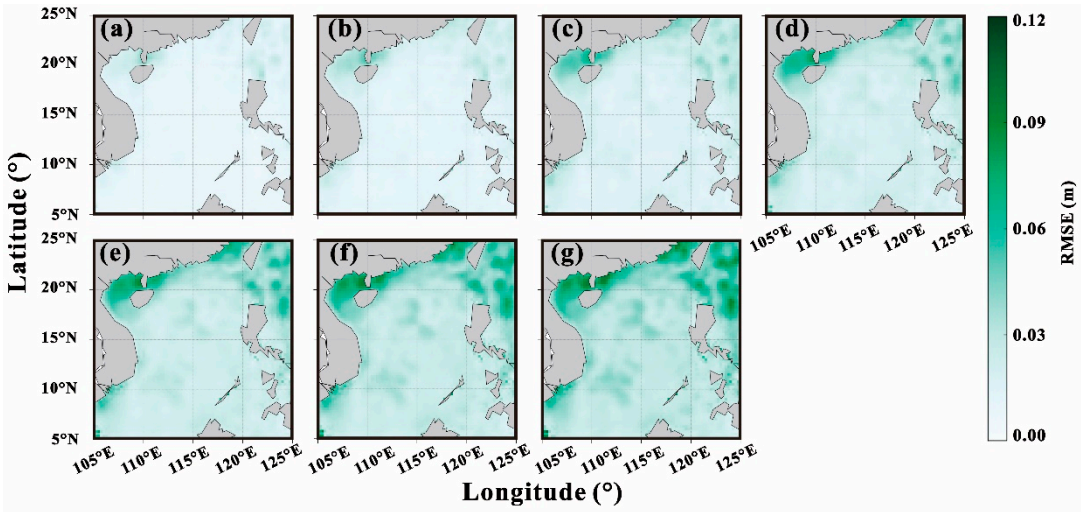

Figure 7. Average root mean square error (RMSE) at each grid point from June to July. (**a**–**g**) The RMSE maps from the first day to the seventh day of prediction.

3.3. Eddy Nowcasting Evaluation

It is insufficient to quantify the prediction ability of the improved Conv-LSTM network for mesoscale eddies based on SLA errors alone. To qualitatively and quantitatively analyse the results of eddy nowcasting experiments, the SLA data are used to identify the eddies and extract the eddy properties. Figure 8 shows the positions and contours of the predicted mesoscale eddies on 2 August, 2018. Blue represents the cyclonic eddies and red represents the anticyclonic eddies. The eddies in Figure 8a were identified from observed SLA data and are regarded true eddies. Figure 8b–h shows the eddies on August 2 based on the nowcasting results from first to seventh day of nowcasts.

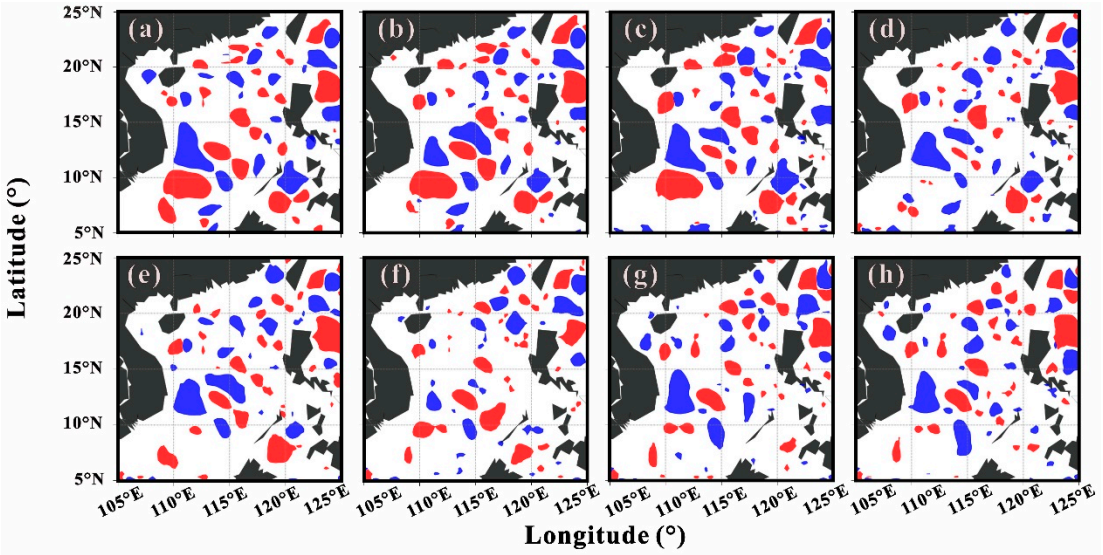

Figure 8. The results of eddy identification based on SLA data on 2 August, 2018. (**a**) Snapshot of true eddies on 2 August, 2018. (**b**–**h**) Snapshots of predicted eddies from the first day to seventh day of nowcasting. Red represents the anticyclonic eddies and blue represents the cyclonic eddies.

To assess the predictability of eddies, the prediction results of eddies were evaluated, and 92 nowcasting experiments were conducted. Each of the 92 days from June to August 2018 was associated with a set of nowcasting results spanning from the first day to the seventh day of nowcasts. Then, the number of successfully predicted eddies was counted, and their properties were analysed. In the evaluation of the results of eddy nowcasting, four parameters were selected for comparison: The matching ratio of the eddy nowcasting, position errors of the eddies, radius errors of the eddies and amplitude errors of the eddies. The nowcasting results can be divided into three types: Correctly predicted eddies (TP), eddies predicted as non-eddies (FP) and non-eddies predicted as eddies (FN).

In the evaluation of the eddy nowcasting results, it is desirable to omit as few eddies as possible, so we define the matching ratio of eddies as the evaluation standard, as shown in Equation (4).

$$\text{Matching ratio} = \frac{Tp}{Tp + Fn} \tag{4}$$

To determine whether an eddy is correctly predicted, the predictions and observations were compared, and the eddies satisfying the matching conditions were considered correctly predicted. All the true eddies were traversed, and the predicted eddies within 0.5° longitude and latitude of the true eddies were considered eddies corresponding to the true eddies. The assessment formulas are as follows.

$$\left|Lat_{truth[j]} - Lat_{pred[i]}\right| \leq x \;\&\; \left|Lon_{truth[j]} - Lon_{pred[i]}\right| \leq x \tag{5}$$

$$Type_{truth[j]} = Type_{pred[i]} \tag{6}$$

In the above formula, $Lat_{truth[j]}$ and $Lon_{truth[j]}$ are the latitude and longitude of the true eddy centre, and x is the radius of the neighbourhood, which is set to 0.5° in this experiment. $Type_{truth[j]}$ and $Type_{pred[i]}$ are the polarity (cyclonic versus anticyclonic) of the true eddy and predicted eddy, respectively, which must be equal to satisfy the assessment criterion. If two conditions are satisfied, $\text{Eddy}_{pred[j]}$ corresponds to $\text{Eddy}_{truth[j]}$. When there is more than one predicted eddy in the study area that can be matched with the same true eddy, the nearest eddy is selected as the matching result. To clearly visualize the matching results, all results are plotted in a graph. Circle with radius equivalent to those of the eddies are created, with the centre of each eddy as the origin. The eddies in the same colour correspond to the same real eddy. The results from 2 August, 2018, are shown in Figure 9.

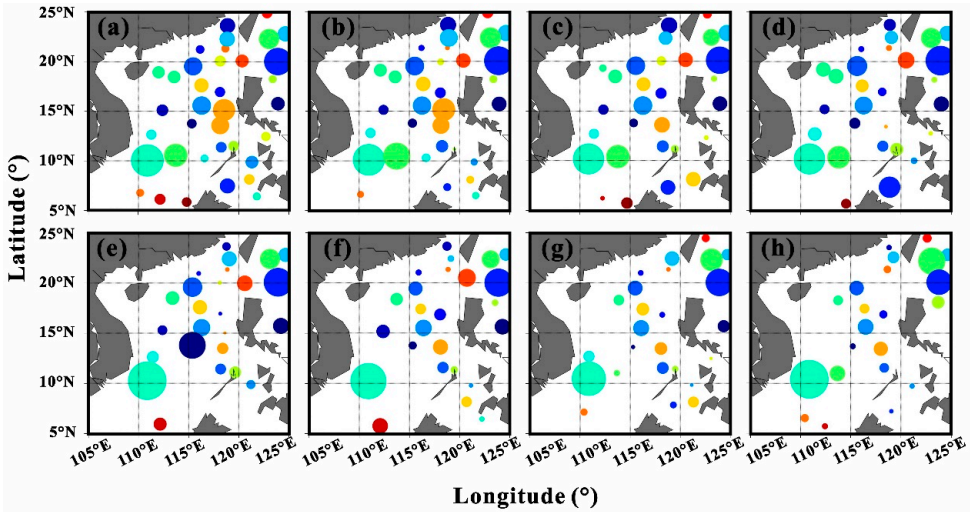

Figure 9. Radiuses and positions for the eddy matching results on 2 August 2018. (**a**) The radiuses and positions of real eddies identified from observed SLA data on 2 August (**b**–**h**) The radiuses and positions of eddies that correspond to true eddies on 1st day to 7th day of nowcasts. The eddies of the same colour are regarded as matched to the same true single eddy.

Figure 10 shows the influences of the eddy diameter and prediction time on the forecasting performance. As the time-step length increases, the number of eddies that can be successfully predicted decreases, the position of the eddy centre gradually deviates, and the radius and amplitude errors gradually increase. From the first day to the seventh day of predictions, the matching ratio decreases from 83% to 46%, and the quality of the prediction also decreases. With the extension of the nowcasting time steps, the eddy signals contained in the SLA prediction results is increasingly lost, which leads to a decline in the prediction quality.

As the eddy radius increases, the matching ratio increases. On the first day of nowcasts, the matching ratio for eddies with a diameter of greater than 100 km reaches 95%, and the average matching ratio for seven-day nowcasting is 80%. As the radius increases, the eddy position generated by the successfully predicted eddies also decreases. As the diameter increases to 200 km, the eddy position error decreases from 24 km to 20 km. This result shows that the model loses the signals of the small-radius eddies during the prediction process, which indicates that the model has a better prediction ability for eddies with larger radius. The generation and development processes of large-diameter eddies are more stable and less affected by nonlinear factors than are those of small-diameter eddies, which is conducive to accurate predictions. For eddies with weak kinetic energy and small radius, the prediction model struggles to reproduce and accurately predict their positions. However, the radius and amplitude errors continuously increase as the diameter increases to 200 km. Specifically, the amplitude error increases from 2 cm to 3.5 cm, and the radius error increases from 20 km to 33 km. This result is observed because the radius and amplitude errors are related to their absolute values, and eddies with small radiuses and amplitudes yield relatively small errors.

At the same time, in order to better confirm the validity of the prediction network for the eddy dataset, especially the effectiveness of the unstable stage, we conducted a prediction experiment on the South China Sea eddy dataset from June to August 2015. The purpose of this experiment is to verify the effect of the eddy life stage on the prediction ability. The 2015 eddy dataset was chosen to ensure that there are eddies in each life stage. In the experiment, the prediction error of each stage in the life cycle is counted at intervals of one tenth of the life cycle. The experimental results are shown in Figure 11, where the errors are from the first day prediction. Among them, the matching ratio starts to rise from the eddy formation period and steeply drops during the eddy disappearance stage. The other three errors have the same trend, starting a slight fall after the formation stage and significantly rise

during the disappearance stage. The matching ratio at formation stage is around 0.78, and then it is held steady at about 0.83. Finally, it drops to 0.66 at the stage of disappearance.

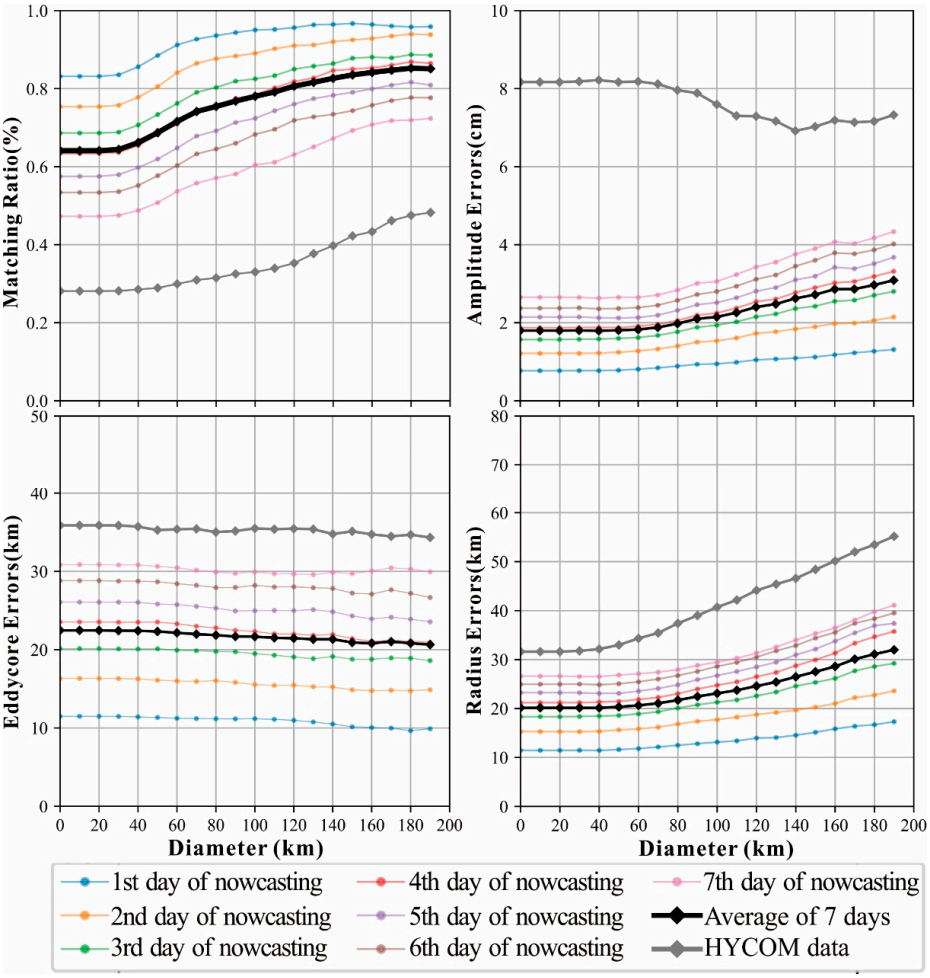

Figure 10. The relation between predicted eddy properties and eddy diameters as well as the comparison between eddy parameters predicted by deep neural network and those extracted from HYCOM data. The black bold lines are the average values of the seven-day predictions. The grey lines are the values of HYCOM data.

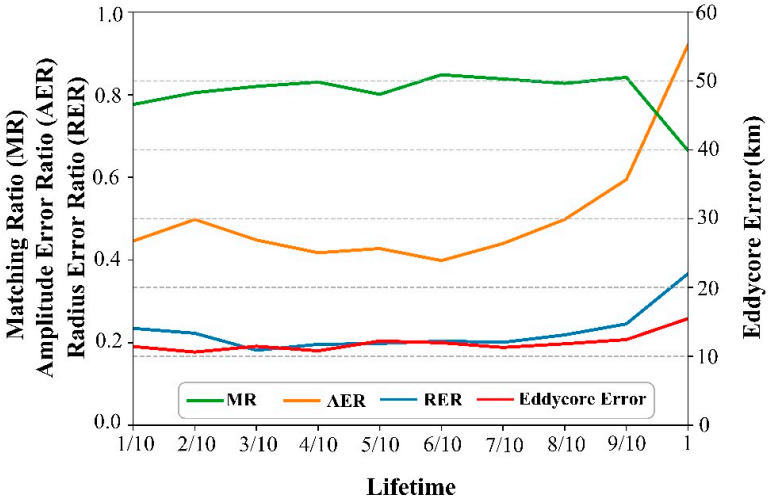

Figure 11. The relation between life stage and nowcasting errors.

As shown in Figure 11, the amplitude has the largest error and the error increases during the stage of disappearance. Figure 12a is the distribution of the eddy amplitude in the eddy data set used in the experiment. This means that a large part of the eddies has a very small amplitude, which makes the prediction difficult. It is notable that very small amplitudes can result in large error ratios and increase overall error. In response to this, we selected eddies with amplitude greater than 1 cm in the dataset, and the prediction result of these eddies is shown in Figure 12b. It can be concluded that eddies with small amplitude in the data set are the main factor of prediction error.

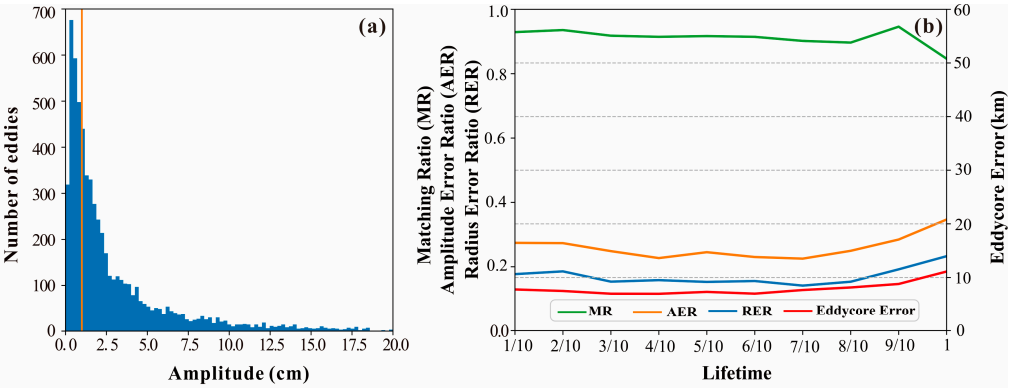

Figure 12. (**a**) Amplitude distribution in eddy data set, the red vertical line indicates the amplitude equal to 1 cm. (**b**) The relation between life stages and nowcasting errors of eddies with amplitude more than 1 cm.

A comparison of the errors of cyclonic and anticyclonic eddies (Table 1) indicates that the polarities of the eddies have little effect on the prediction ability of the model. Additionally, the ability to predict mesoscale eddies depends on the size of the mesoscale eddies to a certain extent.

Table 1. Nowcasting errors of cyclonic and anticyclonic eddies.

		Nowcasting Days							HYCOM
		1st	2nd	3rd	4th	5th	6th	7th	
Matching Ratio (%)	Anticyclonic eddies	79.8	70.4	64.6	58.0	52.2	47.3	40.4	21.9
	Cyclonic eddy	76.1	67.7	59.6	51.4	44.8	40.4	35.0	19.0
Amplitude Errors (cm)	Anticyclonic eddies	0.8	1.3	1.7	2.0	2.3	2.6	2.9	8.7
	Cyclonic eddy	0.7	1.1	1.4	1.7	2.0	2.1	2.4	7.7
Eddycore Errors (km)	Anticyclonic eddies	11.3	16.0	20.2	23.8	26.1	28.6	30.6	36.5
	Cyclonic eddy	11.7	16.7	20.1	23.2	26.0	29.1	31.2	35.2
Radius errors (km)	Anticyclonic eddies	11.9	15.9	19.0	21.4	23.3	25.5	27.4	30.7
	Cyclonic eddy	10.9	14.6	17.6	20.9	23.1	24.3	25.6	32.5

4. Discussion

4.1. Verification with an Anticyclonic Eddy Shedding from Kuroshio

The Kuroshio intrudes into the South China Sea through the Luzon Strait with the waters of the Northwest Pacific Ocean, making an important contribution to the dynamic, thermal and salt balance of the South China Sea [35]. The eddy shedding from the Kuroshio is an important way for the Kuroshio's penetration in the South China Sea [36]. Therefore, it is very valuable to predict the eddy shedding process in Luzon Strait using the prediction model to better understand the characteristics of these eddies. The Kuroshio intrusion is seasonal. The frequency of the circulation path in southwestern Taiwan in winter is higher than that in other seasons, and the anticyclonic eddies often separate from the circulation path. From the SLA data on January 2017, it can be observed that the Kuroshio

penetrates the interior of the South China Sea and separates an anticyclonic eddy with a radius of 100 km. The shedding process is presented in Figure 13.

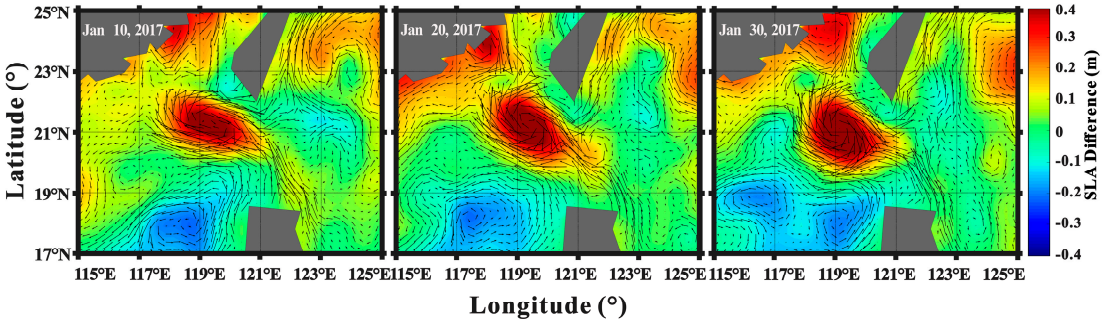

Figure 13. SLA and surface current fields from AVISO data in January 2017. The target anticyclonic eddy shed from the Kuroshio in January 2017.

The shedding eddy continued to develop, moving westward from the Luzon Strait and continuing to disappear into the middle of the South China Sea in June 2017. The eddy formed in November 2016 and shed from the Kuroshio in January 2017, with the trajectory ranging from 119.3°E, 21.2°N to 113.3°E, 17.3°N. In each day of the lifetime of the anticyclonic eddy, a seven-day nowcast based on the previous 30 days observations is performed on the eddy. The comparison between the predicted results of one seven-day nowcast and the true parameters of this anticyclonic eddy is shown in Figure 14. From 30 January to 5 February, the error of eddy centres is 4 km, 3.5 km, 7.7 km, 8.4 km, 5.5 km, 5.4 km and 4.4 km, respectively. Figure 15 shows the prediction errors in the whole lifecycle of the anticyclonic eddy. The errors of radius and amplitude are relatively large in the initial stage of the eddy and fluctuate within a certain range in the development and extinction stages. The average radius error ratio of the whole life cycle is 0.07 (radius error/radius absolute value), and the average amplitude error ratio is 0.10 (amplitude error/amplitude absolute value). Before entering the South China Sea, this anticyclonic eddy was still unstable, and the error of the eddy centre fluctuated greatly from the 40th to the 80th day of its lifetime. The maximum value appeared in this stage, and the average distance error of the eddy centres was 11.2 km. After the anticyclonic eddy entered the South China Sea, the prediction error of this anticyclonic eddy was relatively stable. The radius error ratio increased around 125th day, mainly because the eddy radius observed by the altimeter changed sharply. In this case, it is difficult for the network to predict radius accurately.

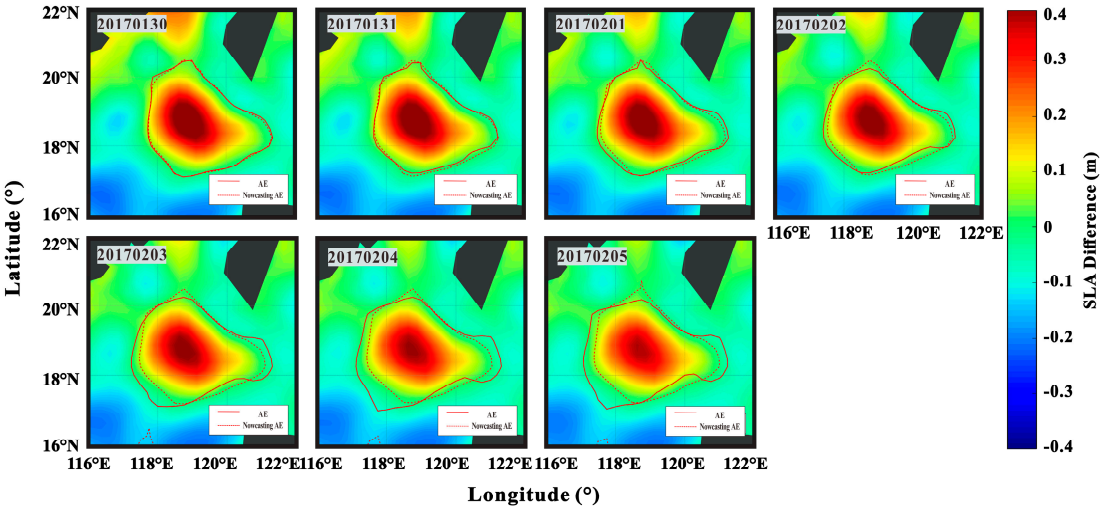

Figure 14. The results of the seven-day nowcasting of the target anticyclonic eddy on 30 January 2017. The background is the predicted SLA values, the solid lines are the true eddy contours and the dotted lines are the predictions.

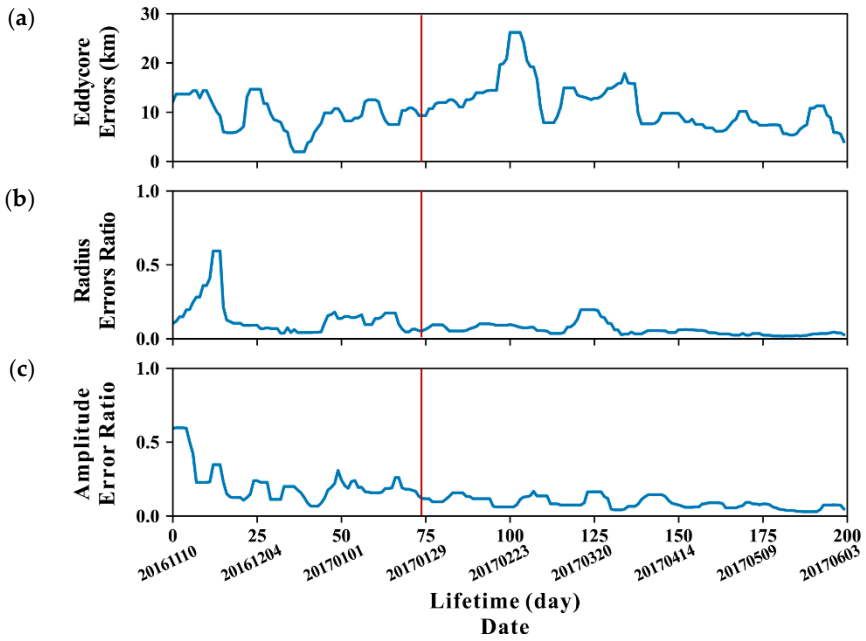

Figure 15. Time series of the errors of the eddy positions (**a**), radius (**b**) and amplitude (**c**). The red line is the time when the eddy separated from the Kuroshio.

From the nowcasting results of the anticyclonic eddy shedding from the Kuroshio, it can be seen that the deep neural network can reproduce the anticyclonic eddy from the development to the maturity and then begin to decline and can reproduce its movement from northeast to southwest route. Its lifetime process has little influence on the nowcast effect.

4.2. Comparison with HYCOM Data

To further verify the validity of the experiment, HYCOM data are used to conduct an eddy detection experiment, and the results are compared with those based on the AVISO data. HYCOM is part of the Global Ocean Data Assimilation Experiment (GODAE) of the United States. The Navy Coupled Ocean Data Assimilation System (NCODA) is used to assimilate the existing satellite altimeter observations, Argo profiles and other observation data [37]. The data range is 80.48°S to 80.48°N and 0°E to 360° E. The data are interpolated to a 0.08° grid with a temporal resolution of one day. The data are selected in the same latitude and longitude range as the eddy nowcasting experiment (105–125°E, 5–25°N), totalling 250 × 250 grids. The same detection algorithm as used for the AVISO SLA data is applied to extract the eddy signals. The identification results are shown in Figure 16. The eddies identified from the HYCOM data are matched and compared with the observed eddies, and the analysis results have been added to Figure 10. The statistical results show that there is a large difference between the HYCOM model data and AVISO observation data at the scale of mesoscale eddies. Significantly fewer eddies are identified from the HYCOM data than from the AVISO SLA data, and only 28% eddies can be successfully matched. Additionally, the position and radius errors are larger than those of the predicted eddies, and these errors are larger than the average errors for seven-day nowcasting. Moreover, the amplitudes of the eddies from HYCOM are obviously overestimated. However, the relationship between the errors and eddy radiuses in the HYCOM model is consistent with that of the nowcasting data. Eddies with large radiuses have small eddy position errors and are easier to reproduce than are small-diameter eddies.

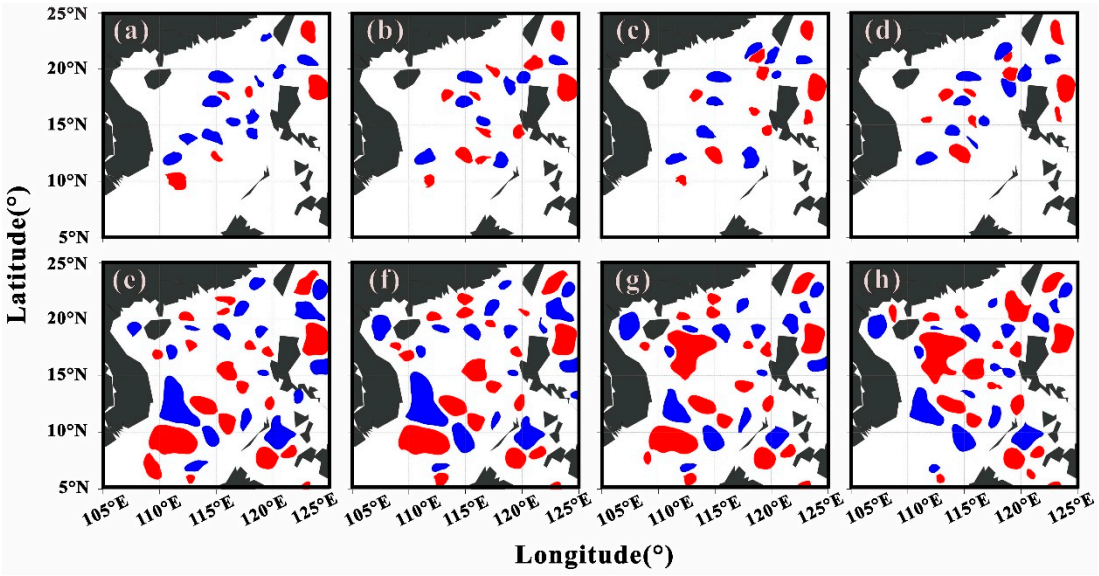

Figure 16. Eddy detection results from 1 August to 4 August, 2018: (**a**–**d**) The eddies detected from HYCOM data, (**e**–**h**) The eddies detected from AVISO satellite altimeter observation data (diameter greater than 75 km). Red represents the anticyclonic eddies and blue represents the cyclonic eddies.

4.3. Comparison with Trajectory Extrapolation

To compare the experimental results, a simple eddy trajectory extrapolation was conducted. The trajectories of the eddy cores over the last 30 days were linearly fit, and the corresponding positions were extrapolated over the next seven days. The eddy centre errors are calculated as the distance between the extrapolated positions and the real positions. The extrapolation errors and errors of the deep learning network model nowcasting results are shown in Figure 17.

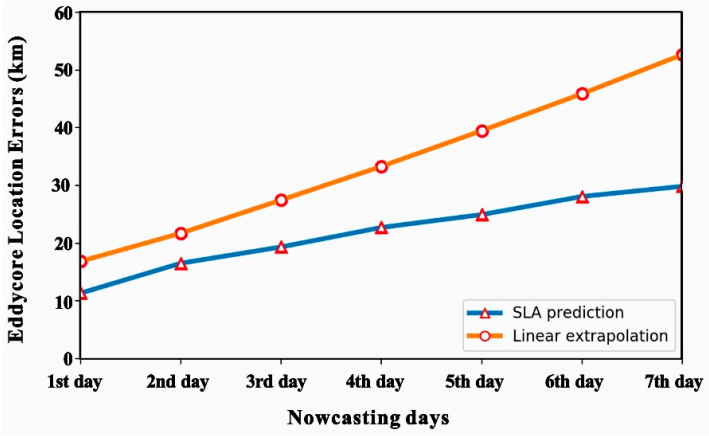

Figure 17. Eddy center position errors of prediction results corresponding to different methods. The orange line represents errors of trajectory linear extrapolation and the blue line represents errors of nowcasting network.

A prediction experiment was performed on eddy trajectory using the LSTM network. Eddies with lifetimes more than 30 days from 1992 to 2015 were selected, and a total of 4582 eddies were obtained to set up the dataset. In the experiment, the eddy positions of the i to i+7 day were used to predict the eddy positions of the i+7~i+14 day. Finally, the distance between the predicted position and the actual position in the dataset is calculated and averaged. The error of seven-day position prediction using LSTM was about 36 km, while that of prediction using Conv-LSTM was 21 km. The results highlight the advantage of the Conv-LSTM network in nowcasting the positions of eddies.

5. Conclusions

The purpose of this paper is to perform eddy nowcasting using a deep neural network, which is different from the traditional model of using various environmental and physical data. In this study, only the time series data collected by remote sensing altimeters are used as inputs, and an empirical model is established using an improved Conv-LSTM network to output the future SLA maps. The parameters of the eddies in the SLA data are extracted with an eddy detection method. The predicted eddies are matched with the observed eddies, which were regarded as true eddies. The statistical and comparative results show that the deep neural network can successfully nowcast eddies. On the first day of nowcasts, the matching ratio for eddies with diameters greater than 100 km reached 95%. However, the nowcasting performance suffers a slightly decay for the long term, and the average performance over seven days of nowcasts is approximately 60%. The neural network does not display obvious differences in its nowcasting ability for cyclonic and anticyclonic eddies, but the radius of the eddies has a considerable influence on the nowcasting results. The probability that eddies with larger diameters can be successfully predicted is higher, and the position errors of the eddy centres are smaller, indicating that the nowcasting results depend on the size of the eddy to some extent.

The eddy nowcasting method is based entirely on the Conv-LSTM network and the SLA data set, without any eddy-related prior information. In order to test the ability of nowcasting algorithm to reproduce individual eddies, we selected a typical anticyclonic eddy shedding from Kuroshio and carried out nowcasting experiments on it. It can be seen from the experimental results that the improved Conv-LSTM network can well reproduce the development and propagation of this eddy, with the average error of eddy centre is 11.2 km. The predicted eddy parameters are compared with those detected from the HYCOM data set to obtain comparable results. The number of eddies that HYCOM data can reproduce is significantly less than the number of eddies predicted by the deep learning network. Specifically, only 28% of true eddies are identified from HYCOM data set, and the positions of the eddy centres also deviate more from the positions of the true eddy centres, and the deviations can exceed 35 km. The HYCOM data set significantly overestimates the eddy amplitudes. At the mesoscale, the ocean eddies predicted by the improved Conv-LSTM networks are closer to the true eddies than eddies identified from HYCOM data.

Author Contributions: Conceptualization, C.M. and G.C.; Data curation, J.Y.; Formal analysis, C.M. and S.L.; Funding acquisition, G.C.; Investigation, C.M. and S.L.; Methodology, C.M. and S.L.; Project administration, G.C.; Resources, J.Y.; Software, A.W.; Supervision, G.C.; Validation, J.Y.; Visualization, A.W.; Writing—original draft, S.L.; Writing—review & editing, C.M.

Funding: This research was funded by the Marine S&T Fund of Shandong Province for Pilot National Laboratory for Marine Science and Technology (Qingdao): No. 2018SDKJ0102-8, Fundamental Research Funds for the Central Universities: No. 201762005, National Key Scientific Instrument and Equipment Development Projects of National Natural Science Foundation of China: No. 41527901.

Conflicts of Interest: The authors declare no conflict of interest.

References

1. Zhang, Y.; Liu, Z.; Zhao, Y.; Wang, W.; Li, J.; Xu, J. Mesoscale eddies transport deep-sea sediments. *Sci. Rep.* **2014**, *4*, 5937. [CrossRef] [PubMed]
2. Cotroneo, Y.; Aulicino, G.; Ruiz, S.; Pascual, A.; Budillon, G.; Fusco, G.; Tintore, J. Glider and satellite high resolution monitoring of a mesoscale eddy in the Algerian basin: Effects on the mixed layer depth and biochemistry. *J. Mar. Syst.* **2015**, *162*, 72–88. [CrossRef]
3. Font, J.; Isern-Fontanet, J.; Salas, J.J. Tracking a big anticyclonic eddy in theWestern Mediterranean Sea. *Sci. Mar.* **2004**, *68*, 331–342. [CrossRef]
4. Olita, A.; Ribotti, A.; Sorgente, R.; Fazioli, L.; Perilli, A. SLA-chlorophyll-a variability and covariability in the Algero-Proven çal Basin (1997–2007) through combined use of EOF and wavelet analysis of satellite data. *Ocean Dyn.* **2011**, *61*, 89–102. [CrossRef]

5. Pujol, M.I.; Larnicol, G. Mediterranean Sea eddy kinetic energy variability from 11 years of altimetric data. *J. Mar. Syst.* **2005**, *58*, 121–142. [CrossRef]
6. Aulicino, G.; Cotroneo, Y.; Lacava, T.; Sileo, G.; Fusco, G.; Carlon, R.; Satriano, V.; Pergola, N.; Tramutoli, V.; Budillon, G. Results of the first wave glider experiment inthe southern Tyrrhenian Sea. *Adv. Oceanogr. Limnol.* **2016**, *7*, 16–35. [CrossRef]
7. Aulicino, G.; Cotroneo, Y.; Ruiz, S.; Sánchez Román, A.; Pascual, A.; Fusco, G.; Tintor e, J.; Budillon, G. Monitoring the Algerian Basin through glider observations, satellitealtimetry and numerical simulations along a SARAL/AltiKa track. *J. Mar. Syst.* **2018**, *179*, 55–71. [CrossRef]
8. Pessini, F.; Olita, A.; Cotroneo, Y.; Perilli, A. Mesoscale eddies in the Algerian Basin: Do they differ as a function of their formation site? *Ocean Sci.* **2018**, *14*, 669–688. [CrossRef]
9. Cotroneo, Y.; Aulicino, G.; Ruiz, S.; Sánchez Román, A.; Torner Tomàs, M.; Pascual, A.; Fusco, G.; Heslop, E.; Tintoré, J.; Budillon, G. Glider data collected during the Algerian Basin Circulation Unmanned Survey. *Earth Syst. Sci. Data* **2019**, *11*, 147–161. [CrossRef]
10. Ansorge, I.; Jackson, J.; Reid, K.; Durgadoo, J.; Swart, S.; Eberen, S. Evidence of a southward eddy corridor in the south-west Indian ocean. *Deep-Sea Res.* **2014**, *119*, 69–76. [CrossRef]
11. Cotroneo, Y.; Budillon, G.; Fusco, G.; Spezie, G. Cold core eddies and fronts of the Antarctic Circumpolar Current south of New Zealand from in situ and satellite data. *J. Geophys. Res. Ocean.* **2013**, *118*, 2653–2666. [CrossRef]
12. Holland, W. The role of mesoscale eddies in the general circulation of the ocean—Numerical experiments using a wind-driven quasigeo-strophic model. *J. Phys. Oceanogr.* **1978**, *8*, 363–392. [CrossRef]
13. Holland, W.R.; Lin, L.B. On the origin of mesoscale eddies and their contribution to the general circulation of the ocean. I. A preliminary numerical experiment. *J. Phys. Oceanogr.* **1975**, *5*, 642–657. [CrossRef]
14. Keffer, T.; Holloway, G. Estimating Southern Ocean eddy flux of heat and salt from satellite altimetry. *Nature* **1988**, *332*, 624–626. [CrossRef]
15. Morrow, R.; Donguy, J.R.; Chaigneau, A.; Rintoul, S.R. Cold core anomalies at the subantarctic front, south of Tasmania. *Deep Sea Res.* **2004**, *51*, 1417–1440. [CrossRef]
16. Robinson, A.R.; Carton, J.A.; Mooers, C.N.K.; Walstad, L.J.; Carter, E.F.; Rienecker, M.M.; Smith, J.A.; Leslie, W.G. A real-time dynamical forecast of ocean synoptic/mesoscale eddies. *Nature* **1984**, *309*, 781. [CrossRef]
17. Masina, S.; Pinardi, N. Mesoscale data assimilation studies in the Middle Adriatic Sea. *Cont. Shelf Res.* **1994**, *14*, 1293–1310. [CrossRef]
18. Shriver, J.F.; Hurlburt, H.E.; Smedstad, O.M.; Wallcraft, A.J.; Rhodes, R.C. 1/32 real-time global ocean prediction and value-added over 1/16 resolution. *J. Mar. Syst.* **2007**, *65*, 3–26. [CrossRef]
19. Smedstad, O.M.; Hurlburt, H.E.; Metzger, E.J.; Rhodes, R.C.; Shriver, J.F.; Wallcraft, A.J.; Kara, A.B.; Murray, C.P. An operational real-time eddy-resolving 1/16° global ocean nowcast/forecast system. In Proceedings of the OCEANS'02 MTS/IEEE, Biloxi, MI, USA, 29–31 October 2002; Volume 2, pp. 769–774.
20. Isern-Fontanet, J.; García-Ladona, E.; Font, J. Identification of marine eddies from altimetric maps. *J. Atmos. Ocean. Technol.* **2003**, *20*, 772–778. [CrossRef]
21. Isern-Fontanet, J.; García-Ladona, E.; Font, J. Vortices of the Mediterranean Sea: An altimetric perspective. *J. Phys. Oceanogr.* **2006**, *36*, 87–103. [CrossRef]
22. Chelton, D.B.; Schlax, M.G.; Samelson, R.M. Global observations of nonlinear mesoscale eddies. *Prog. Oceanogr.* **2011**, *91*, 167–216. [CrossRef]
23. Lima, E.; Sun, X.; Dong, J.; Wang, H.; Yang, Y.; Liu, L. Learning and transferring convolutional neural network knowledge to ocean front recognition. *IEEE Geosci. Remote Sens. Lett.* **2017**, *14*, 354–358. [CrossRef]
24. Yang, Y.; Dong, J.; Sun, X.; Lima, E.; Mu, Q.; Wang, X. A CFCC-LSTM model for sea surface temperature prediction. *IEEE Geosci. Remote Sens. Lett.* **2018**, *15*, 207–211. [CrossRef]
25. Hochreiter, S.; Schmidhuber, J. Long short-term memory. *Neural Comput.* **1997**, *9*, 1735–1780. [CrossRef]
26. Karpathy, A.; Li, F. Deep visual-semantic alignments for generating image descriptions. *IEEE Trans. Pattern Anal. Mach. Intell.* **2017**, *39*, 664–676. [CrossRef]
27. Donahue, J.; Anne Hendricks, L.; Guadarrama, S.; Rohrbach, M.; Venugopalan, S.; Saenko, K.; Darrell, T. Long-term recurrent convolutional networks for visual recognition and description. *IEEE Trans. Pattern Anal. Mach. Intell.* **2017**, *39*, 677–691. [CrossRef]

28. Xingjian, S.H.I.; Chen, Z.; Wang, H.; Yeung, D.Y.; Wong, W.K.; Woo, W.C. Convolutional LSTM Network: A machine learning approach for precipitation nowcasting. In Proceedings of the Advances in Neural Information Processing Systems, Montreal, QC, Canada, 7–12 December 2015; pp. 802–810.
29. Liu, Y.; Chen, G.; Sun, M.; Liu, S.; Tian, F. A Parallel SLA-Based Algorithm for Global Mesoscale Eddy Identification. *J. Atmos. Ocean. Technol.* **2016**, *33*, 2743–2754. [CrossRef]
30. Wang, G.; Su, J.; Chu, P.C. Mesoscale eddies in the South China Sea observed with altimeter data. *Geophys. Res. Lett.* **2003**, *30*. [CrossRef]
31. Chen, G.; Hou, Y.; Chu, X.; Qi, P. Vertical structure and evolution of the Luzon Warm Eddy. *Chin. J. Oceanol. Limnol.* **2010**, *28*, 955–961. [CrossRef]
32. Du, Y.; Wu, D.; Liang, F.; Yi, J.; Mo, Y.; He, Z.; Pei, T. Major migration corridors of mesoscale ocean eddies in the South China Sea from 1992 to 2012. *J. Mar. Syst.* **2016**, *158*, 173–181. [CrossRef]
33. Chen, G.; Hou, Y.; Chu, X. Mesoscale eddies in the South China Sea: Mean properties, spatiotemporal variability, and impact on thermohaline structure. *J. Geophys. Res. Ocean.* **2011**, *116*. [CrossRef]
34. Lotter, W.; Kreiman, G.; Cox, D. Deep Predictive Coding Networks for Video Prediction and Unsupervised Learning. *arXiv* **2016**, arXiv:1605.08104.
35. Jia, Y.; Liu, Q.; Liu, W. Primary study of the mechanism of eddy shedding from the Kuroshio bend in Luzon Strait. *J. Oceanogr.* **2005**, *61*, 1017–1027. [CrossRef]
36. Nan, F.; Xue, H.; Yu, F. Kuroshio intrusion into the South China Sea: A review. *Prog. Oceanogr.* **2015**, *137*, 314–333. [CrossRef]
37. Cummings, J.A.; Smedstad, O.M. Variational Data Assimilation for the Global Ocean. In *Data Assimilation for Atmospheric, Oceanic and Hydrologic Applications (Vol. II)*; Springer-Verlag: Berlin/Heidelberg, Germany, 2013; pp. 303–343.